

On the Benefits of Memory for Modeling Time-Dependent PDEs

Ricardo Buitrago Ruiz¹, Tanya Marwah¹, Albert Gu^{1,2}, and Andrej Risteski¹

¹Machine Learning Department, Carnegie Mellon University

²Cartesia AI

{ricardob, tmarwah, agu, aristeski}@andrew.cmu.edu

Abstract

Data-driven techniques have emerged as a promising alternative to traditional numerical methods for solving partial differential equations (PDEs). These techniques frequently offer a better trade-off between computational cost and accuracy for many PDE families of interest. For time-dependent PDEs, existing methodologies typically treat PDEs as Markovian systems, i.e., the evolution of the system only depends on the “current state”, and not the past states. However, distortion of the input signals — e.g., due to discretization or low-pass filtering — can render the evolution of the distorted signals non-Markovian. In this work, motivated by the Mori-Zwanzig theory of model reduction, we investigate the impact of architectures with memory for modeling PDEs: that is, when past states are explicitly used to predict the future. We introduce Memory Neural Operator (MemNO), a network based on the recent SSM architectures and Fourier Neural Operator (FNO). We empirically demonstrate on a variety of PDE families of interest that when the input is given on a low-resolution grid, MemNO significantly outperforms the baselines without memory, achieving more than $6\times$ less error on unseen PDEs. Via a combination of theory and experiments, we show that the effect of memory is particularly significant when the solution of the PDE has high frequency Fourier components (e.g., low-viscosity fluid dynamics), and it also increases robustness to observation noise.

1 Introduction

Time-dependent partial differential equations (PDEs) are central to modeling various scientific and physical phenomena, necessitating the design of accurate and computationally efficient solvers. Recently, data-driven neural network based approaches [Li et al., 2021b, Lu et al., 2019] have emerged as an attractive alternative to classic numerical solvers, such as finite element and finite difference methods [LeVeque, 2007]. Classical approaches are computationally expensive in high dimension, and struggle with PDEs which are very sensitive to initial conditions. Learned approaches can often negotiate these difficulties better, at least for the family of PDEs they are trained on.

One example of a data-driven approach is learning a *neural solution operator*, which for a time-dependent PDE learns a time evolution map that predicts the solution of the PDE for future time steps. The operators are frequently autoregressively parametrized, such that the network predicts future states based on previous ones [Li et al., 2021a, 2022], and the number of past states the model is conditioned on serves as “memory” and is treated as a tunable hyperparameter. Recent works [Tran et al., 2023, Lippe et al., 2023] suggest that optimal performance across various PDE families can be achieved by conditioning the models only on the immediate past state—i.e., treating the system as Markovian—though this is in settings in which the training data is very high-resolution.

In many practical settings, we expect to only observe a part of the system. This could be due to limited resolution of the measurement devices collecting the data, inherent observational errors in the system, or

prohibitive computational difficulty generating high-quality synthetic data. This can lead to significant information loss, particularly in systems like turbulent flows [Pope, 2001] or shock formation in fluid dynamics [Christodoulou, 2007], where PDEs change abruptly in space and time. In such situations, classical results from dynamical systems (Mori-Zwanzig theory), suggest that the system becomes strongly non-Markovian.

More precisely, Mori-Zwanzig theory [Mori, 1965, Zwanzig, 1961, Ma et al., 2018] is an ansatz to understand the evolution of a subspace of system (e.g., the top k Fourier components). Under certain conditions, this evolution can be divided into a *Markovian term* (the evolution of the chosen subspace under the PDE), a *memory term* (which is a weighted sum of the values of all previous iterates in the chosen subspace), and an “*unobservable*” term, which depends on the values of the initial conditions orthogonal to the chosen subspace.

In this paper, we study the effects of explicit memory when deploying neural operators for time-dependent PDEs. By memory we loosely mean a representation of the previous states of a PDE. We focus on PDE families that take the form $\partial_t u(x, t) = \mathcal{L}u(x, t)$ where $u(x, t) : \Omega \times [0, T] \rightarrow \mathbb{R}$ is a time-dependent function defined over the domain Ω , and \mathcal{L} is a (possibly non-linear) operator. This is a generic form of a time-dependent PDE system and contains many PDE families of interest in different application domains (e.g., heat diffusion, Navier-Stokes, Kuramoto-Sivashinsky, Black-Scholes, Schrödinger equation to name a few).

We introduce **Memory Neural Operator (MemNO)**, an architecture which combines Fourier neural operator (FNO) [Li et al., 2021a, Tran et al., 2023] and the S4 architecture [Gu et al., 2022, 2023]. The MemNO architecture can be seen as an adaptation of the FNO [Li et al., 2021b] architecture where the FNO layers model the spatial dynamics of the PDE while the S4 layers [Gu et al., 2022, 2023] maintain a compressed memory of the past states. We choose S4 models over recurrent architectures like LSTM [Hochreiter and Schmidhuber, 1997] due to superior performance in modeling long range dependencies [Gu et al., 2022, Tay et al., 2020], ease of training, and favorable memory and computational scaling with both state dimension and sequence length. Through our experiments we show that for PDEs observed on low resolution grids and/or with observation noise, MemNO outperforms their Markovian (memoryless) baselines—achieving $6\times$ less loss on unseen PDEs. Our contributions are as follows:

- We introduce MemNO, a Memory Neural Operator architecture which uses a *combination of FNO layers and S4 layers* to model the spatial and temporal dynamics of a PDE. The S4 layers explicitly model memory, by introducing a weighted average over the past (compressed) states.
- Even in relatively simple linear PDEs, we theoretically show the *memory term can result in a solution that is (arbitrarily) closer to the correct solution*, compared to the Markovian approximation — in particular when the operator describing the PDE “mixes” the observed and unobserved subspace.
- Across several families of one-dimensional and two-dimensional PDEs, we show that when the input is supplied on a *low-resolution grid*, or has additional *observation noise*, memory based architectures outperform the best performing FNO based baselines by a significant margin.
- Finally, we empirically show that this effect is more pronounced for PDEs which result in *solutions with high order frequency modes*, and introduce a metric which indicates when memory based models will have most impact.

2 Related Work

Data-driven neural solution operators [Chen and Chen, 1995, Bhattacharya et al., 2021, Lu et al., 2019, Kovachki et al., 2023] have emerged as the dominant approach for approximating PDEs, given their ability to model multiple families of PDEs at once, and relatively fast computation at inference time.

Recently, many architectures have been proposed to improve the performance of neural operators across multiple families of PDEs, Li et al. [2021a] designed the Fourier Neural Operator (FNO), a resolution

invariant architecture that uses a convolution based integral kernels evaluated in the Fourier space. [Tran et al. \[2023\]](#) later introduced Factorized FNO (FFNO) architecture, that builds upon and improves the FNO architecture by adding separable spectral layers and residual connections. Additionally, they perform extensive ablations that point out that strategies like the Markov assumption—i.e., predicting a state only from its immediate prior state—is optimal and outperforms models that use the history of past timesteps as input. [Lippe et al. \[2023\]](#) performed a similar study for long rollouts of the PDE solution and concluded the the optimal performance is indeed achieved under the Markovian assumption. However, we show that when there is a loss of information in the observation a PDE, a model that the uses the history of past states outperforms its Markovian counterpart, often achieving $6\times$ less error on unseen PDEs from the same family.

Our work is motivated by the Mori-Zwanzig formalism [[Zwanzig, 1961](#), [Mori, 1965](#)] which shows that a partial observation of the current state of the system can be compensated using memory of past states. Our work is also inspired by a previous study on the effects of memory in modeling PDE dynamics by [[Ma et al., 2018](#)]. Here the authors draw parallels to the Mori-Zwanzig equations and LSTM [[Hochreiter and Schmidhuber, 1997](#)] to model the dynamics of the top Fourier components of a time-dependent 1D Kuramoto-Sivashinsky and 2D shear flow equations, one single PDE at a time. However, in our work, we study the benefits of memory in neural operator settings, i.e, we have a single model that learns the dynamics of an entire family of PDE at once. Furthermore, we use the S4 state space model architecture [[Gu et al., 2022](#)] to model the temporal dependencies, which in our experiments has better performance and is more stable than LSTMs.

3 Preliminaries

In this section, we introduce several definitions, as well as background on the Mori-Zwanzig formalism as applied to our setting.

3.1 Partial Differential Equations (PDEs)

Definition 1 (Space of square integrable functions). For integers d, V and an open set $\Omega \subset \mathbb{R}^d$, we define $L^2(\Omega; \mathbb{R}^V)$ as the space of square integrable functions $u : \Omega \rightarrow \mathbb{R}^V$ such that $\|u\|_{L^2} \leq \infty$, where $\|u\|_{L^2} = \left(\int_{\Omega} \|u(x)\|_2^2 dx\right)^{\frac{1}{2}}$.

Notation 1 (Restriction). Given a function $u : \Omega \rightarrow \mathbb{R}^V$ and a subset $A \subset \Omega$, we denote $u|_A$ as the restriction of u to the domain A , i.e. $u|_A : A \rightarrow \mathbb{R}^V$.

The general form the PDEs we consider in this paper will be as follows:

Definition 2 (Time-Dependent PDE). For an open set $\Omega \subset \mathbb{R}^d$ and an interval $[0, T] \subset \mathbb{R}$, a Time-Dependent PDE is the following expression:

$$\frac{\partial u}{\partial t}(t, x) = \mathcal{L}[u](t, x), \quad \forall t \in [0, T], x \in \Omega, \quad (1)$$

$$u(0, x) = u_0(x), \quad \forall x \in \Omega, \quad (2)$$

$$\mathcal{B}[u|_{\partial\Omega}](t) = 0, \quad \forall t \in [0, T] \quad (3)$$

where $\mathcal{L} : L^2(\Omega; \mathbb{R}^V) \rightarrow L^2(\Omega; \mathbb{R}^V)$ is a differential operator in x which is independent of time, $u_0(x) \in L^2(\Omega; \mathbb{R}^V)$ and \mathcal{B} is an operator defined on the boundary of $\partial\Omega$, commonly referred as the boundary condition.

Unless otherwise stated, both in the experiments and in the theory we will largely work with *periodic* boundary conditions:

Definition 3 (Periodic Boundary Conditions). For $\Omega = [0, L]^d$, we define the periodic boundary conditions as the condition:

$$u(x_1, \dots, x_{k-1}, 0, x_{k+1}, \dots, x_d) = u(x_1, \dots, x_{k-1}, L, x_{k+1}, \dots, x_d)$$

for all $(x_1, \dots, x_{k-1}, x_{k+1}, \dots, x_L) \in [0, L]^{d-1}$ and all $k = 1, \dots, d$.

Finally, we will frequently talk about a grid of a given resolution:

Definition 4 (Equispaced grid with resolution f). Let $\Omega = [0, L]^d$. An equispaced grid with resolution f in Ω is the following set $\mathcal{S} \subset \mathbb{R}^d$:

$$\mathcal{S} = \left\{ \left(i_1 \frac{L}{f}, \dots, i_k \frac{L}{f} \right) \mid 0 \leq i_k \leq f-1 \text{ for } 1 \leq k \leq d \right\}.$$

We will also denote by $|\mathcal{S}|$ the number of points in \mathcal{S} .

3.2 Mori-Zwanzig

The Mori-Zwanzig formalism [Zwanzig, 2001] deals with cases where an equation is known for a full system, yet only a part of it is observed. It leverages the knowledge of past observed states of a system to compensate for the loss of information that arises from the partial observation. In our paper, partial observation can refer to observing the solution at a discretized grid in space or only observing the Fourier modes up to a critical frequency. In particular, the Mori-Zwanzig formalism in the context of time-dependent PDEs is well-known in the Physics literature as the Nakajima-Zwanzig equation ([Nakajima, 1958])

Now, we will apply the Nakajima-Zwanzig equation to our setting. Assume we have a PDE as in Definition 2. Let $\mathcal{P} : L^2(\Omega; \mathbb{R}^V) \rightarrow L^2(\Omega; \mathbb{R}^V)$ be a linear projection operator. We define $\mathcal{Q} = I - \mathcal{P}$, where I is the identity operator. In our setting, for the PDE solution at timestep t $u_t \in L^2(\Omega; \mathbb{R}^V)$, $\mathcal{P}[u_t]$ is the part of the solution that we observe and $\mathcal{Q}[u_t]$ is the unobserved part. Thus, the initial information we receive for the system is $\mathcal{P}[u_0]$. Applying \mathcal{P} and \mathcal{Q} to Equation 1 and using $u = \mathcal{P}[u] + \mathcal{Q}[u]$, we get:

$$\frac{\partial}{\partial t} \mathcal{P}[u](t, x) = \mathcal{P}\mathcal{L}[u](t, x) = \mathcal{P}\mathcal{L}\mathcal{P}[u](t, x) + \mathcal{P}\mathcal{L}\mathcal{Q}[u](t, x) \quad (4)$$

$$\frac{\partial}{\partial t} \mathcal{Q}[u](t, x) = \mathcal{Q}\mathcal{L}[u](t, x) = \mathcal{Q}\mathcal{L}\mathcal{P}[u](t, x) + \mathcal{Q}\mathcal{L}\mathcal{Q}[u](t, x) \quad (5)$$

Solving for 5 yields $\mathcal{Q}[u](t, x) = \int_0^t \exp\{\mathcal{Q}\mathcal{L}(t-s)\} \mathcal{Q}\mathcal{L}\mathcal{P}[u](s, x) ds + e^{\mathcal{Q}\mathcal{L}t} \mathcal{Q}[u_0](t, x)$.

Plugging into 4, we obtain a *Generalized Langevin Equation* [Mori, 1965] for $\mathcal{P}[u]$:

$$\frac{\partial}{\partial t} \mathcal{P}[u](t, x) = \mathcal{P}\mathcal{L}\mathcal{P}[u](t, x) + \mathcal{P}\mathcal{L} \int_0^t \exp\{\mathcal{Q}\mathcal{L}(t-s)\} \mathcal{Q}\mathcal{L}\mathcal{P}[u](s, x) ds + \mathcal{P}\mathcal{L} e^{\mathcal{Q}\mathcal{L}t} \mathcal{Q}[u_0](t, x) \quad (6)$$

We will refer to the first summand on the right hand side of 6 as the **Markovian** term because it only depends on $\mathcal{P}[u](t, x)$, the second summand as the **memory** term because it depends on $\mathcal{P}[u](s, x)$ for $0 \leq s \leq t$, and the third summand as the **unobserved residual** as it depends on $\mathcal{Q}[u_0]$ which is never observed.

We note that Equation 6 is exact, not an approximation, so it is equivalent to solving the full system. Typically, the term that is most difficult to compute is the exponential of the memory term, and thus several methods to approximate it have been proposed. In the physics literature, the memory term has been approximated through a perturbation expansion of the exponential [Breuer and Petruccione, 2002], or by approximating the operator $\exp\{\mathcal{Q}\mathcal{L}(t-s)\} : L^2(\Omega; \mathbb{R}^V) \rightarrow L^2(\Omega; \mathbb{R}^V)$ through operators defined in $\mathcal{P}[L^2(\Omega; \mathbb{R}^V)]$ [Shi and Geva, 2003, Zhang et al., 2006, Montoya-Castillo and Reichman, 2016, Kelly et al., 2016]. In the machine learning literature, Ma et al. [2018] develop the equations for the case when the operator \mathcal{P} kept only the top-k modes, and designed a hybrid approach where the memory term was approximated with an LSTM [Hochreiter and Schmidhuber, 1997], and then used as an additional input of a numerical solver. In this work, we treat the whole memory term as an operator $\mathcal{M} : \mathcal{C}([0, T], \mathcal{P}[L^2(\Omega; \mathbb{R}^V)]) \rightarrow \mathcal{P}[L^2(\Omega; \mathbb{R}^V)]$ ¹ to be learnt by a parametrized sequential layer of a Neural Operator.

¹Here $\mathcal{C}(A, B)$ denotes the space of continuous functions $u : A \rightarrow B$.

4 Our approach

4.1 Training procedure

First, we describe the high-level training scaffolding for our method, namely the way the data is generated, and the loss we use.

Training data: Let $u \in \mathcal{C}([0, T]; L^2(\Omega; \mathbb{R}^V))$ be the solution of the PDE given by Definition 2. Let \mathcal{S} be an equispaced grid in Ω with resolution f , and let \mathcal{T} be another equispaced grid in $[0, T]$ with $N_t + 1$ points. Given $u_0(x)_{|\mathcal{S}}$, our goal is to predict $u(t, x)_{|\mathcal{S}}$ for $t \in \mathcal{T}$ using a Neural Operator.

Training loss: As it is standard, we proceed through empirical risk minimization on a dataset of trajectories. More specifically, given a loss function $\ell : (\mathbb{R}^{|\mathcal{S}|}, \mathbb{R}^{|\mathcal{S}|}) \rightarrow \mathbb{R}$, a dataset of training trajectories $(u(t, x)^{(i)})_{i=0}^N$, and parametrized maps $\mathcal{G}_t^\Theta : \mathbb{R}^{|\mathcal{S}|} \rightarrow \mathbb{R}^{|\mathcal{S}|}$ for $t \in \mathcal{T}$, we define:

$$\Theta^* = \min_{\Theta} \frac{1}{N} \sum_{i=0}^{N-1} \frac{1}{N_t} \sum_{t=1}^{N_t} \ell(u(t, x)_{|\mathcal{S}}, \mathcal{G}_t^\Theta[u_0(x)_{|\mathcal{S}}])$$

We then aim to find an adequate architecture choice such that \mathcal{G}^{Θ^*} has low test error on unseen trajectories of the same PDE.

4.2 The Architecture: Memory Neural Operator

In this section we describe Memory Neural Operator (MemNO), a Deep Learning framework to incorporate memory into Neural Operators. Let NO_t^Θ be a Neural Operator with L layers, and denote $\text{NO}_t^\Theta[u_0]$ the prediction of the solution of the PDE at time t . We will assume that this Neural Operator follows the Markovian assumption, i.e. we can write:

$$\text{NO}_{t_{i+1}}^\Theta[u_0] = r_{\text{out}} \circ \ell_L \circ \ell_{L-1} \circ \dots \circ \ell_0 \circ r_{\text{in}}[\text{NO}_{t_i}^\Theta[u_0]] \quad (7)$$

Where $r_{\text{in}} : \mathbb{R}^{|\mathcal{S}|} \rightarrow \mathbb{R}^{|\mathcal{S}| \times h_0}$ and $r_{\text{out}} : \mathbb{R}^{|\mathcal{S}| \times h_{L+1}} \rightarrow \mathbb{R}^{|\mathcal{S}|}$ are projector operators; $\ell_j : \mathbb{R}^{|\mathcal{S}| \times h_j} \rightarrow \mathbb{R}^{|\mathcal{S}| \times h_{j+1}}$ are parametrized layers; and h_j is the dimension of the j -th hidden layer.

Our goal is to define a network \mathcal{G}_t^Θ that builds upon NO_t^Θ and can incorporate memory. For this we take inspiration from the Mori-Zwanzig theory exposed in Section 3.2. Comparing Equation 7 with Equation 6, we identify $\ell_L \circ \ell_{L-1} \circ \dots \circ \ell_0$ with the Markov term which models the spatial dynamics. To introduce the memory term, we interleave an additional residual sequential layer \mathcal{M} that acts on hidden representations of the solution at previous timesteps. Concretely, the MemNO architecture can be written as:

$$\mathcal{G}_{t_{i+1}}^\Theta[u_0] = \mathcal{R}_{\text{out}} \circ \mathcal{L}_L \circ \dots \circ \mathcal{L}_{k+1} \circ \mathcal{M} \circ \mathcal{L}_k \circ \dots \circ \mathcal{L}_0 \circ \mathcal{R}_{\text{in}}[\mathcal{G}_{t_i}^\Theta[u_0], \mathcal{G}_{t_{i-1}}^\Theta[u_0], \dots, u_0]$$

Where $-1 \leq k \leq L$ is a chosen hyperparameter.² Now, the spatial \mathcal{L}_j layers are understood to be applied timestep-wise. That is, if $v^{(j)}(t')$ is the hidden representation at the j layer for a timestep $t' \leq t_i$, then $\mathcal{L}_{j+1}[v^{(j)}(t_i), \dots, v^{(j)}(t_0)] = [\ell_j[v_i^{(j)}(t_i)], \dots, \ell_j[v_0^{(j)}(t_0)]]$, and analogously for \mathcal{R}_{in} and \mathcal{R}_{out} . Thus, the \mathcal{L}_j layers still follow the Markovian assumption. The memory is introduced through \mathcal{M} , which consists of a sequential layer m that is applied to the time history of the hidden representation of the k -th layer, that is $\mathcal{M} : \mathbb{R}^{i \times |\mathcal{S}| \times h_k} \rightarrow \mathbb{R}^{|\mathcal{S}| \times h_k}$ with $(\mathcal{M}[v^{(k)}(t_i), \dots, v^{(k)}(t_0)])_{sh} = m[v_{sh}^{(k)}(t_i), \dots, v_{sh}^{(k)}(t_0)]$. Note that m is the same for each of the $|\mathcal{S}| \times h_k$ elements of the hidden layer. The main motivation of our MemNO framework is that it can be utilized with *any* existing neural operator layer ℓ , and with any (causal) sequential model \mathcal{M} . Thus it provides a modular architecture design which we hope can serve as a useful tool for practitioners.

² $k = L$ refer to inserting M after all the S layers, and $k = -1$ refers to inserting M as the first layer. As we show in Appendix F.2, our experiments are not very sensitive to the choice of k .

5 Theoretical motivation for memory: a simple example

In this section, we provide a simple, but natural example of a (linear) PDE, along with (in the nomenclature of Section 3.2) a natural projection operator given by a *Fourier truncation measurement operator*, such that the memory term in the generalized Langevin equation (GLE) can have an arbitrarily large impact on the quality of the calculated solution. We will work with periodic functions over $[0, 2\pi]$ which have a convenient basis:

Definition 5 (Basis for 2π -periodic functions). A function $f : \mathbb{R} \rightarrow \mathbb{R}$ is 2π -periodic if $f(x + 2\pi) = f(x)$. We can identify 2π -periodic functions with functions over the torus $T := \{e^{i\theta} : \theta \in \mathbb{R}\} \subseteq \mathbb{C}$ by the map $\tilde{f}(e^{ix}) = f(x)$. Note that $\{e^{inx}\}_{n \in \mathbb{Z}}$ is a basis for the set of 2π -periodic functions.

We will define the following measurement operator:

Definition 6 (Fourier truncation measurement). The operator $\mathcal{P}_k : L^2(T; \mathbb{R}) \rightarrow L^2(T; \mathbb{R})$ acts on $f \in L^2(T; \mathbb{R})$, $f(x) = \sum_{n=-\infty}^{\infty} a_n e^{inx}$ as $\mathcal{P}_k(f) = \sum_{n=-k}^k a_n e^{inx}$.

We will also define for notational convenience the functions $\{\mathbf{e}_n\}_{n \in \mathbb{Z}}$, where $\mathbf{e}_n(x) := e^{-inx} + e^{inx}$. Now we consider the following operator to define a linear time-dependent PDE:

Proposition 1. Let $\mathcal{L} : L^2(T; \mathbb{R}) \rightarrow L^2(T; \mathbb{R})$ be defined as $\mathcal{L}u(x) = -\Delta u(x) + B \cdot (e^{-ix} + e^{ix})u(x)$ for $B > 0$. Then, we have:

$$\forall 1 \leq n \in \mathbb{N}, \quad \mathcal{L}(\mathbf{e}_n) = n^2 \mathbf{e}_n + B(\mathbf{e}_{n-1} + \mathbf{e}_{n+1}) \quad \& \quad \mathcal{L}(\mathbf{e}_0) = 2B\mathbf{e}_1$$

The crucial property of this operator is that it acts by “mixing” the n -th Fourier basis with the $(n-1)$ -th and $(n+1)$ -th: thus information is propagated to both the higher and lower-order part of the spectrum. Given the above proposition, we can easily write down the evolution of a PDE with operator \mathcal{L} in the basis $\{\mathbf{e}_n\}_{n \in \mathbb{Z}}$:

Proposition 2. Let \mathcal{L} be defined as in Proposition 1. Consider the PDE

$$\begin{aligned} \frac{\partial}{\partial t} u(t, x) &= \mathcal{L}u(t, x) \\ u(0, x) &= \sum_{n \in \mathbb{N}_0} a_n(0) \mathbf{e}_n \end{aligned}$$

Let $u(t, x) = \sum_{n \in \mathbb{N}_0} a_n^{(t)} \mathbf{e}_n$. Then, the coefficients $a_n^{(t)}$ satisfy:

$$\forall 1 \leq n \in \mathbb{N}, \quad \frac{\partial}{\partial t} a_n^{(t)} = n^2 a_n^{(t)} + B \left(a_{n-1}^{(t)} + a_{n+1}^{(t)} \right) \quad (8)$$

$$\frac{\partial}{\partial t} a_0^{(t)} = 2B a_1^{(t)} \quad (9)$$

With this setup in mind, we will show that as B grows, the memory term in Equation 6 can have an arbitrarily large effect on the calculated solution:

Theorem 1 (Effect of memory). Consider the Fourier truncation operator \mathcal{P}_1 and let $\mathcal{Q} = I - \mathcal{P}_1$. Let $u(0, x)$ have the form in Proposition 2 for $B > 0$ sufficiently large, and let $a_n^{(0)} > 0, \forall n > 0$. Consider the memoryless and memory-augmented PDEs:

$$\frac{\partial u_1}{\partial t} = \mathcal{P}_1 \mathcal{L} u_1 \quad (10)$$

$$\frac{\partial u_2}{\partial t} = \mathcal{P}_1 \mathcal{L} u_2 + \mathcal{P}_1 \mathcal{L} \int_0^t \exp\{\mathcal{Q} \mathcal{L}(t-s)\} \mathcal{Q} \mathcal{L} u_2(s) ds \quad (11)$$

with $u_1(0, x) = u_2(0, x) = \mathcal{P}_1 u(0, x)$. Then, u_1 and u_2 satisfy:

$$\forall t > 0, \|u_1(t) - u_2(t)\|_{L_2} \gtrsim Bt \|u_1(t)\|_{L_2} \quad (12)$$

$$\forall t > 0, \|u_1(t) - u_2(t)\|_{L_2} \gtrsim Bt \exp(\sqrt{2}Bt) \quad (13)$$

Remark 1. Note that the two conclusions of the theorem mean that both the absolute difference, and the relative difference between the PDE including the memory term Equation 11 and not including the memory term Equation 10 can be arbitrarily large as $B, t \rightarrow \infty$.

Remark 2. The choice of \mathcal{L} is made for ease of calculation of the Markov and memory term. Conceptually, we expect the solution to Equation 11 will differ a lot from the solution to Equation 10 if the action of the operator \mathcal{L} tends to “mix” components in the span of \mathcal{P} and the span of \mathcal{Q} .

Remark 3. If we solve the equation $\frac{\partial}{\partial t} u(t, x) = \mathcal{L}u(t, x)$ exactly, we can calculate that $\|u(t)\|_{L_2}$ will be on the order of $\exp(2Bt)$. This can be seen by writing the evolution of the coefficients of $u(t)$ in the

basis $\{\mathbf{e}_n\}$, which looks like: $\frac{\partial}{\partial t} \begin{pmatrix} a_0 \\ a_1 \\ \dots \end{pmatrix} = \mathcal{O} \begin{pmatrix} a_0 \\ a_1 \\ \dots \end{pmatrix}$ where \mathcal{O} is roughly a tridiagonal Toeplitz operator

$$\mathcal{O} = \begin{pmatrix} & \vdots & \vdots & \vdots & \vdots \\ \dots & B & n^2 & B & 0 & \dots \\ \dots & 0 & B & (n+1)^2 & B & \dots \\ & \vdots & \vdots & \vdots & \vdots \end{pmatrix}. \text{ The largest eigenvalue of this operator can be shown to be on the}$$

order of at least $2B$ (equation (4) in [Noschese et al., 2013]). The Markov term results in a solution of order $\exp(\sqrt{2}Bt)$ (Equation 18, Equation 19), which is multiplicatively smaller by a factor of $\exp((2 - \sqrt{2})Bt)$. The result in this Theorem shows the memory-based PDE Equation 11 results in a multiplicative “first order” correction which can be seen by Taylor expanding $\exp(\sqrt{2}Bt) \approx 1 + \sqrt{2}Bt + \frac{1}{2}(\sqrt{2}B)^2 t^2 + \dots$.

6 Memory helps with low-resolution data and input noise: a case study

In this section we present a case study for several common PDEs of practical interest, showing that MemNO brings accuracy benefits when the data is supplied in low resolution. Through our experiments we show the difference in the performance between a baseline “memoryless” architecture, which we choose to be Factorized Fourier Neural Operator (FFNO) [Tran et al., 2023] and a memory-augmented architecture using S4 [Gu et al., 2022], which we denote as the S4-Factorized Fourier Neural Operator (s4FFNO). The architectural details for both the architectures are elaborated upon in Appendix B.

6.1 Setup: Training and evaluation procedure

To construct our datasets, we first produce discretized trajectories of a PDE for N_t timesteps, i.e. $(u(t))_{t=0}^{N_t}$ in a *high resolution* discretized spatial grid $\mathcal{S}^{HR} \subset \mathbb{R}^d$, i.e. $u(t) \in \mathbb{R}^{|\mathcal{S}^{HR}|}$. We then produce datasets that consist of *lower resolution* versions of the above trajectories, i.e. on a grid \mathcal{S}^{LR} of lower resolution f . For 1-dimensional datasets, the discretized trajectory on \mathcal{S}^{LR} is obtained by cubic interpolation of the trajectory in the high resolution grid. In 2D, the discretized trajectory is obtained by downsampling. We will show results in different resolutions, in which case both train and test trajectories are at such resolution, and the loss function is also computed at the chosen resolution. Our training loss and evaluation metric is *normalized Root Mean Squared Error (nRMSE)*:

$$\text{nRMSE}(u(t, x)_{|\mathcal{S}^{LR}}, \hat{u}(t)) = \frac{\|u(t, x)_{|\mathcal{S}^{LR}} - \hat{u}(t)\|_2}{\|u(t, x)_{|\mathcal{S}^{LR}}\|_2},$$

where $\|\cdot\|_2$ is the euclidean norm in $\mathbb{R}^{|\mathcal{S}^{HR}|}$. More details on training are given in appendix E.

6.2 Kuramoto–Sivashinsky equation (1D): a study in low-resolution

The Kuramoto–Sivashinsky equation (KS) is a nonlinear PDE that is used as a modeling tool in fluid dynamics, chemical reaction dynamics, and ion interactions. Due to its chaotic behavior it can model instabilities in various physical systems. For a viscosity ν , it is written as $u_t + uu_x + u_{xx} + \nu u_{xxxx} = 0$. We generated datasets for KS at different viscosities and resolutions. The results are shown in Table 1. We can see s4FFNO outperforms FFNO across these viscosities and resolutions, having an nRMSE that can be more than six times smaller. We also note that, since the memory layer is applied element-wise in the time dimension, it has very few parameters compared to the spatial layers, as seen in the difference of parameters between s4FFNO and FFNO in column 3.

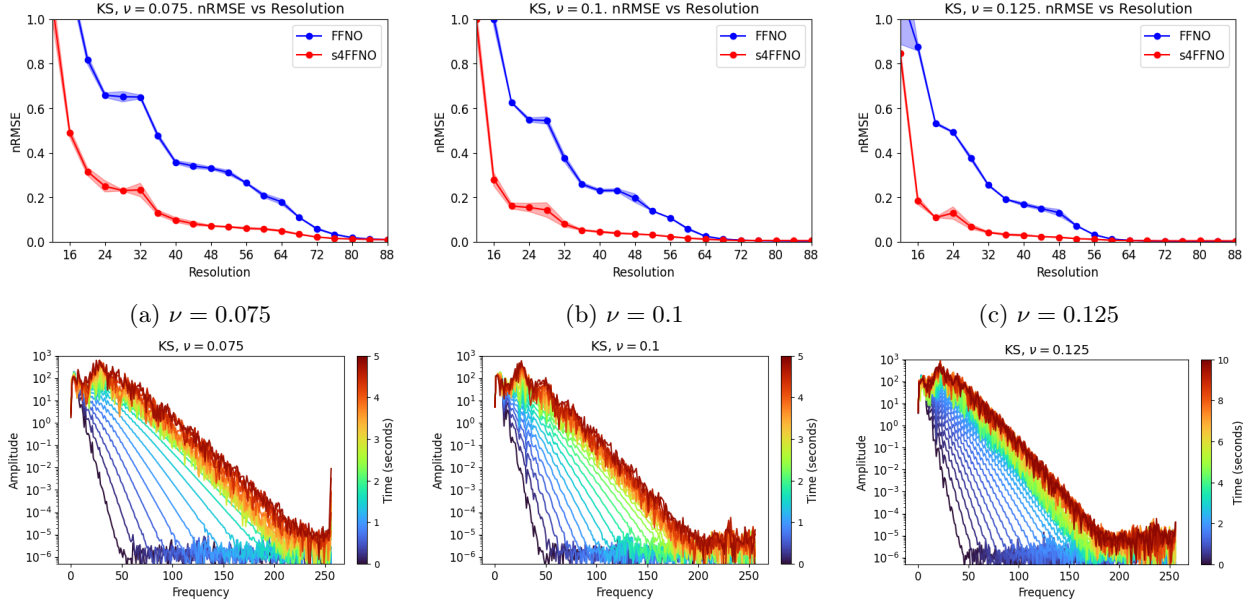


Figure 1: (First row) nRMSE for FFNO and s4FFNO in the KS dataset at different resolutions, where each column is a different viscosity. The final time is $T = 5s$ and there are $N_t = 25$ timesteps. The average of three runs with different seeds is shown and the shaded area shows the standard deviation. (Second row) A visualization of the whole frequency spectrum at each of the 25 timesteps for a single trajectory in the dataset. The spectrum is obtained with the ground truth solution at resolution 512, and it is smoothed with a Gaussian filter with 0.4 standard deviation for better visualization.

Architecture	Resolution	Parameters	nRMSE ↓			
			$\nu = 0.075$	$\nu = 0.1$	$\nu = 0.125$	$\nu = 0.15$
FFNO	32	2.79M	0.650	0.376	0.254	0.187
FFNO	48	3.84M	0.330	0.196	0.131	0.068
FFNO	64	4.89M	0.179	0.024	0.006	0.003
s4FFNO	32	2.85M	0.233	0.079	0.042	0.028
s4FFNO	48	3.90M	0.071	0.035	0.020	0.010
s4FFNO	64	4.94M	0.049	0.011	0.005	0.003

Table 1: nRMSE values at different resolutions for KS with different viscosities. The final time is 5 seconds and the trajectories contain 25 timesteps.

The key factor for the improved performance of MemNO over memoryless Neural Operators is not the absolute resolution, but rather the *resolution relative to the frequency spectrum of the solution*. The lower the viscosity, the higher the frequencies that appear in the spectrum. This can be clearly seen in Figure 1: in the

top row, as viscosities increase, the resolution at which there is a significant difference between s4FFNO and FFNO decreases. In the second row of the figure, we show a visualization of the frequency spectrum of a solution at those viscosities.

We note that even if the initial condition does not contain high frequencies, in the KS equation high frequencies will appear as the system evolves—indeed, this dataset was generated with initial conditions whose maximum Fourier mode was 8. This is in qualitative agreement with the theoretical motivation in Section 5—albeit the KS equation is substantially more complicated since it is nonlinear, so it is hard to fully theoretically analyze. We provide a similar study on 1D Burgers equation in the Appendix C.

6.3 Navier Stokes equation (2D): study in observation noise

The Navier Stokes equation describes the motion of a viscous fluid. Like in Li et al. [2021a], we consider the incompressible form in the 2D unit torus, which is given by:

$$\begin{aligned} \frac{\partial w(x, t)}{\partial t} + u(x, t) \cdot \nabla w(x, t) &= \nu \Delta w(x, t) + f(x), & x \in (0, 1)^2, t \in (0, T] \\ \nabla \cdot u(x, t) &= 0, & x \in (0, 1)^2, t \in [0, T] \\ w(x, 0) &= w_0(x), & x \in (0, 1)^2 \end{aligned}$$

Where $w = \nabla \times u$ is the vorticity, $w_0 \in L^2((0, 1)^2; \mathbb{R})$ is the initial vorticity, $\nu \in \mathbb{R}_+$ is the viscosity coefficient, and $f \in L^2((0, 1)^2; \mathbb{R})$ is the forcing function. In general, the lower the viscosity, the more rapid the changes in the solution and the harder it is to solve it numerically and with a Neural Operator. We investigate the effect of memory when adding IID Gaussian noise to the inputs of our neural networks. Noise would represent the observation noise arising from the intrinsic error of the measurement device. The noise $\epsilon \in \mathbb{R}^{|\mathcal{T}| \times |\mathcal{S}^{LR}|}$ is sampled IID from a Gaussian distribution $\epsilon_{ts} \sim \mathcal{N}(0, \sigma)$, and then added to training and test inputs. During training, for each trajectory a different noise with the same σ is sampled at each iteration of the optimization algorithm. The targets in training and testing represent our ground truth and are not added noise. In Figure 2a, we show the results for $\nu = 10^{-3}$ when adding noise levels from $\sigma = 0.0$ (no noise) to

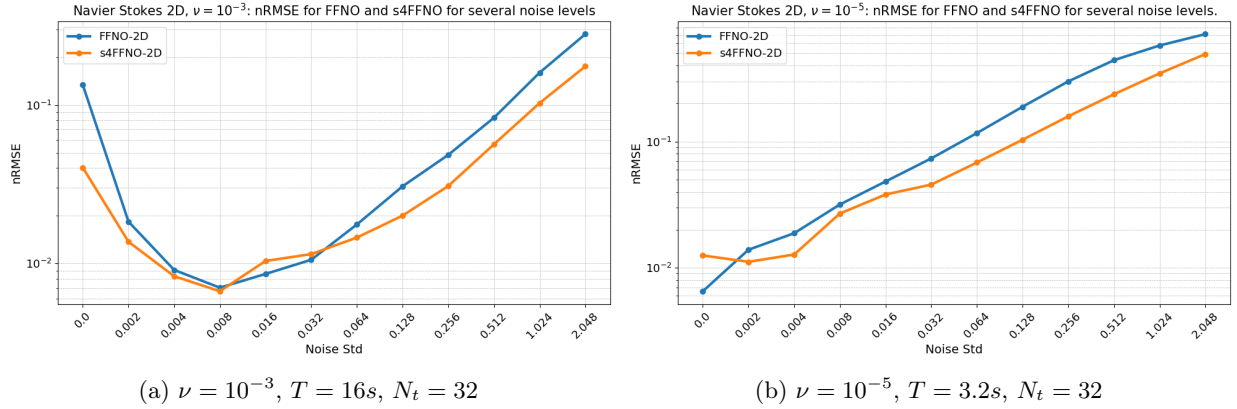


Figure 2: Test nRMSE of FFNO-2D and s4FFNO-2D trained in a Navier Stokes 2D dataset with different noise standard deviations σ added to training and test inputs. Two configurations of viscosity ν , final time T and number of timesteps N_t are shown.

$\sigma = 2.048$. s4FFNO-2D outperforms FFNO-2D across most noise levels, and the difference between the two is especially significant for noise levels beyond 0.128, where FFNO-2D is around 50% higher than s4FFNO-2D (note the logarithmic scale). For this viscosity, adding small levels of noise actually helps training, which was also observed in other settings in Tran et al. [2023]. Figure 2b shows the same experiment performed with $\nu = 10^{-5}$. Again, s4FFNO-2D outperforms FFNO-2D across most noise levels. FFNO-2D losses are similarly around 50% higher for noise levels above 0.032. In this viscosity, adding these levels of noise does not help performance.

6.4 Relationship with fraction of unobserved information

In this section, we provide a simple experiment to quantify the effect of the fraction of unobserved information on the performance of memory based models. Given a grid of resolution f , we define the Fourier truncation measurement $\mathcal{P}_{\lfloor \frac{f}{2} \rfloor}$ as in Section 5, which simply keeps the top $\lfloor \frac{f}{2} \rfloor + 1$ modes and discards the other high frequency modes. Assume $u(t) \in L^2(\Omega; \mathbb{R}^V)$ is the solution of a 1-dimensional PDE at time t , and $a_n^{(t)}$ for $n \in \mathbb{Z}$ is its Fourier Transform. We define the quantity:

$$\omega_f = \frac{1}{N_t} \sum_{i=1}^{N_t} \frac{\sum_{|n| \geq \frac{f}{2}} |a_n^{(t_i)}|^2}{\sum_{n \in \mathbb{Z}} |a_n^{(t_i)}|^2} \quad (14)$$

ω_f is approximate indicator of the amount of information that is lost when the solution of the PDE is observed at resolution f across time. We show that there is a positive correlation between ω_f and the difference in nRMSE between FFNO and s4FFNO for the KS experiment in Figure 3, and also the for Burgers' experiments of Appendix C in Figure 5. This demonstrates the benefits of memory as a way to compensate missing information in the observation.

7 Conclusion and Future Work

We study the benefits of maintaining memory while modeling time dependent PDE systems. Taking inspiration from the Mori-Zwanzig formulation, we show that when we only observe part of the PDE initial condition (for example, PDEs observed on low-resolution or with input noise), the system is no longer Markovian, and the dynamics depend on a *memory term*. To this end, we introduce MemNO, an architecture that combines Fourier Neural Operator (FNO) and the S4 architecture. Through our experiments on different 1D and 2D PDEs, we show that the MemNO architecture outperforms the memoryless baselines.

We present several avenues for future work. First, our experiments on observation noise are limited to the setting where the input noise is IID. Further, extending the experiments and observing the effects of memory in more real-world settings (for example, with non-IID noise or in the presence of aliasing) is a fertile ground for future work, and also necessary to ensure that the application of this method does not have unintended negative consequences when broadly applied in society. Lastly, while we limit our study of the effects of memory to FNO based architectures, performing similar studies for different architectures like Transformer based neural operators [Hao et al., 2023] and diffusion based operators [Lippe et al., 2023] is an interesting direction for future work.

Acknowledgements

RBR is supported by the “la Caixa” Foundation (ID 100010434). The fellowship code is LCF/BQ/EU22/11930090. TM is supported in part by CMU Software Engineering Institute via Department of Defense under contract FA8702-15-D-0002. AR is supported in part by NSF awards IIS-2211907, CCF-2238523, and Amazon Research. The authors also thank Cartesia AI for their generous provision of computational resources.

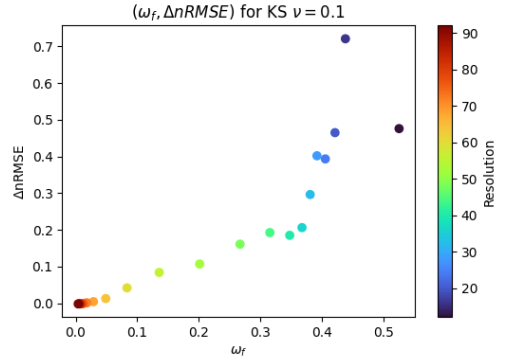


Figure 3: Values of ω_f and the difference in nRMSE between FFNO and s4FFNO for different resolutions in the KS experiment of Section 6.2 with $\nu = 0.1$. ω_f is averaged over all trajectories in the dataset. The value is computed approximating the continuous Fourier modes with Discrete Fourier modes of the solution in the highest resolution available (512 for KS).

References

- Shaojie Bai, J Zico Kolter, and Vladlen Koltun. Deep equilibrium models. *Advances in neural information processing systems*, 32, 2019.
- Maximilian Beck, Korbinian Pöppel, Markus Spanring, Andreas Auer, Oleksandra Prudnikova, Michael Kopp, Günter Klambauer, Johannes Brandstetter, and Sepp Hochreiter. xlstm: Extended long short-term memory, 2024.
- Kaushik Bhattacharya, Bamdad Hosseini, Nikola B Kovachki, and Andrew M Stuart. Model reduction and neural networks for parametric pdes. *The SMAI journal of computational mathematics*, 7:121–157, 2021.
- Johannes Brandstetter, Max Welling, and Daniel E. Worrall. Lie point symmetry data augmentation for neural pde solvers, 2022.
- Heinz-Peter Breuer and Francesco Petruccione. *The Theory of Open Quantum Systems*. Oxford University Press, 2002.
- Shuhao Cao. Choose a transformer: Fourier or galerkin, 2021.
- Tianping Chen and Hong Chen. Universal approximation to nonlinear operators by neural networks with arbitrary activation functions and its application to dynamical systems. *IEEE transactions on neural networks*, 6(4):911–917, 1995.
- Demetrios Christodoulou. *The formation of shocks in 3-dimensional fluids*, volume 2. European Mathematical Society, 2007.
- J. Cooley, P. Lewis, and P. Welch. The finite fourier transform. *IEEE Transactions on Audio and Electroacoustics*, 17(2):77–85, 1969. doi: 10.1109/TAU.1969.1162036.
- Justin Gilmer, Samuel S Schoenholz, Patrick F Riley, Oriol Vinyals, and George E Dahl. Neural message passing for quantum chemistry. In *International conference on machine learning*, pages 1263–1272. PMLR, 2017.
- Albert Gu and Tri Dao. Mamba: Linear-time sequence modeling with selective state spaces. *arXiv preprint arXiv:2312.00752*, 2023.
- Albert Gu, Karan Goel, and Christopher Ré. Efficiently modeling long sequences with structured state spaces. In *The International Conference on Learning Representations (ICLR)*, 2022.
- Albert Gu, Isys Johnson, Aman Timalina, Atri Rudra, and Christopher Re. How to train your HIPPO: State space models with generalized orthogonal basis projections. In *International Conference on Learning Representations*, 2023.
- Jayesh K Gupta and Johannes Brandstetter. Towards multi-spatiotemporal-scale generalized PDE modeling. *Transactions on Machine Learning Research*, 2023. ISSN 2835-8856.
- E. Hairer and G. Wanner. *Solving Ordinary Differential Equations II: Stiff and Differential-Algebraic Problems*. Springer-Verlag, 1996. ISBN 3-540-60452-9.
- Zhongkai Hao, Zhengyi Wang, Hang Su, Chengyang Ying, Yinpeng Dong, Songming Liu, Ze Cheng, Jian Song, and Jun Zhu. Gnot: A general neural operator transformer for operator learning. In *International Conference on Machine Learning*, pages 12556–12569. PMLR, 2023.
- Zhongkai Hao, Chang Su, Songming Liu, Julius Berner, Chengyang Ying, Hang Su, Anima Anandkumar, Jian Song, and Jun Zhu. DPOT: Auto-regressive denoising operator transformer for large-scale PDE pre-training. March 2024. URL <https://github.com/thu-ml/DPOT>.
- Dan Hendrycks and Kevin Gimpel. Gaussian error linear units (GELUs). June 2016. URL <http://arxiv.org/abs/1606.08415>.

- Sepp Hochreiter and Jürgen Schmidhuber. Long Short-Term Memory. *Neural Computation*, 9(8):1735–1780, 11 1997. ISSN 0899-7667. doi: 10.1162/neco.1997.9.8.1735. URL <https://doi.org/10.1162/neco.1997.9.8.1735>.
- Aaron Kelly, Andrés Montoya-Castillo, Lu Wang, and Thomas E. Markland. Generalized quantum master equations in and out of equilibrium: When can one win? *The Journal of Chemical Physics*, 144(18):184105, 05 2016. ISSN 0021-9606. doi: 10.1063/1.4948612. URL <https://doi.org/10.1063/1.4948612>.
- Thomas N Kipf and Max Welling. Semi-supervised classification with graph convolutional networks. *arXiv preprint arXiv:1609.02907*, 2016.
- Nikola Kovachki, Zongyi Li, Burigede Liu, Kamyar Azizzadenesheli, Kaushik Bhattacharya, Andrew Stuart, and Anima Anandkumar. Neural operator: Learning maps between function spaces with applications to pdes. *Journal of Machine Learning Research*, 24(89):1–97, 2023.
- Remi Lam, Alvaro Sanchez-Gonzalez, Matthew Willson, Peter Wirnsberger, Meire Fortunato, Ferran Alet, Suman Ravuri, Timo Ewalds, Zach Eaton-Rosen, Weihua Hu, et al. Graphcast: Learning skillful medium-range global weather forecasting. *arXiv preprint arXiv:2212.12794*, 2022.
- Randall J LeVeque. *Finite difference methods for ordinary and partial differential equations: steady-state and time-dependent problems*. SIAM, 2007.
- Zijie Li, Kazem Meidani, and Amir Barati Farimani. Transformer for partial differential equations’ operator learning. *arXiv preprint arXiv:2205.13671*, 2022.
- Zongyi Li, Nikola Kovachki, Kamyar Azizzadenesheli, Burigede Liu, Andrew Stuart, Kaushik Bhattacharya, and Anima Anandkumar. Multipole graph neural operator for parametric partial differential equations. *Advances in Neural Information Processing Systems*, 33:6755–6766, 2020.
- Zongyi Li, Nikola Kovachki, Kamyar Azizzadenesheli, Burigede Liu, Kaushik Bhattacharya, Andrew Stuart, and Anima Anandkumar. Fourier neural operator for parametric partial differential equations. In *Proceedings of the International Conference on Learning Representations (ICLR)*. ICLR, 2021a.
- Zongyi Li, Hongkai Zheng, Nikola Kovachki, David Jin, Haoxuan Chen, Burigede Liu, Kamyar Azizzadenesheli, and Anima Anandkumar. Physics-informed neural operator for learning partial differential equations. *arXiv preprint arXiv:2111.03794*, 2021b.
- Zongyi Li, Nikola Kovachki, Chris Choy, Boyi Li, Jean Kossaifi, Shourya Otta, Mohammad Amin Nabian, Maximilian Stadler, Christian Hundt, Kamyar Azizzadenesheli, et al. Geometry-informed neural operator for large-scale 3d pdes. *Advances in Neural Information Processing Systems*, 36, 2024.
- Phillip Lippe, Bastiaan S. Veeling, Paris Perdikaris, Richard E Turner, and Johannes Brandstetter. PDE-refiner: Achieving accurate long rollouts with neural PDE solvers. In *Thirty-seventh Conference on Neural Information Processing Systems*, 2023.
- Ilya Loshchilov and Frank Hutter. SGDR: Stochastic gradient descent with warm restarts. In *International Conference on Learning Representations*, 2017.
- Lu Lu, Pengzhan Jin, and George Em Karniadakis. Deeponet: Learning nonlinear operators for identifying differential equations based on the universal approximation theorem of operators. *arXiv preprint arXiv:1910.03193*, 2019.
- Chao Ma, Jianchun Wang, and E Weinan. Model reduction with memory and the machine learning of dynamical systems. August 2018. URL <http://arxiv.org/abs/1808.04258>.
- Tanya Marwah, Ashwini Pople, J Zico Kolter, Zachary Lipton, Jianfeng Lu, and Andrej Risteski. Deep equilibrium based neural operators for steady-state pdes. *Advances in Neural Information Processing Systems*, 36:15716–15737, 2023.

- Michael McCabe, Bruno Régaldo-Saint Blancard, Liam Holden Parker, Ruben Ohana, Miles Cranmer, Alberto Bietti, Michael Eickenberg, Siavash Golkar, Geraud Krawezik, Francois Lanusse, Mariel Pettee, Tiberiu Tesileanu, Kyunghyun Cho, and Shirley Ho. Multiple physics pretraining for physical surrogate models. October 2023. URL <http://arxiv.org/abs/2310.02994>.
- Andrés Montoya-Castillo and David R. Reichman. Approximate but accurate quantum dynamics from the Mori formalism: I. Nonequilibrium dynamics. *The Journal of Chemical Physics*, 144(18):184104, 05 2016. ISSN 0021-9606. doi: 10.1063/1.4948408. URL <https://doi.org/10.1063/1.4948408>.
- Hazime Mori. Transport, collective motion, and brownian motion. *Progress of theoretical physics*, 33(3): 423–455, 1965.
- Sadao Nakajima. On Quantum Theory of Transport Phenomena: Steady Diffusion. *Progress of Theoretical Physics*, 20(6):948–959, 12 1958. ISSN 0033-068X. doi: 10.1143/PTP.20.948. URL <https://doi.org/10.1143/PTP.20.948>.
- Silvia Noschese, Lionello Pasquini, and Lothar Reichel. Tridiagonal toeplitz matrices: properties and novel applications. *Numerical linear algebra with applications*, 20(2):302–326, 2013.
- Antonio Orvieto, Samuel L Smith, Albert Gu, Anushan Fernando, Caglar Gulcehre, Razvan Pascanu, and Soham De. Resurrecting recurrent neural networks for long sequences. In Andreas Krause, Emma Brunskill, Kyunghyun Cho, Barbara Engelhardt, Sivan Sabato, and Jonathan Scarlett, editors, *Proceedings of the 40th International Conference on Machine Learning*, volume 202 of *Proceedings of Machine Learning Research*, pages 26670–26698. PMLR, 23–29 Jul 2023. URL <https://proceedings.mlr.press/v202/orvieto23a.html>.
- Jaideep Pathak, Shashank Subramanian, Peter Harrington, Sanjeev Raja, Ashesh Chattopadhyay, Morteza Mardani, Thorsten Kurth, David Hall, Zongyi Li, Kamyar Azizzadenesheli, et al. Fourcastnet: A global data-driven high-resolution weather model using adaptive fourier neural operators. *arXiv preprint arXiv:2202.11214*, 2022.
- Bo Peng, Eric Alcaide, Quentin Anthony, Alon Albalak, Samuel Arcadinho, Stella Biderman, Huanqi Cao, Xin Cheng, Michael Chung, Matteo Grella, Kranthi Kiran Gv, Xuzheng He, Haowen Hou, Jiaju Lin, Przemyslaw Kazienko, Jan Kocon, Jiaming Kong, Bartlomiej Koptyra, Hayden Lau, Krishna Sri Ipsit Mantri, Ferdinand Mom, Atsushi Saito, Guangyu Song, Xiangru Tang, Bolun Wang, Johan S Wind, Stanislaw Wozniak, Ruichong Zhang, Zhenyuan Zhang, Qihang Zhao, Peng Zhou, Qinghua Zhou, Jian Zhu, and Rui-Jie Zhu. RWKV: Reinventing RNNs for the transformer era. May 2023. URL <http://arxiv.org/abs/2305.13048>.
- Stephen B Pope. Turbulent flows. *Measurement Science and Technology*, 12(11):2020–2021, 2001.
- Md Ashiqur Rahman, Zachary E Ross, and Kamyar Azizzadenesheli. U-NO: U-shaped neural operators. *Transactions on Machine Learning Research*, 2023. ISSN 2835-8856.
- Olaf Ronneberger, Philipp Fischer, and Thomas Brox. U-net: Convolutional networks for biomedical image segmentation. In *Medical image computing and computer-assisted intervention–MICCAI 2015: 18th international conference, Munich, Germany, October 5-9, 2015, proceedings, part III 18*, pages 234–241. Springer, 2015.
- W. E. Schiesser. *The Numerical Method of Lines*. Academic Press, 1991. ISBN 0-12-624130-9.
- Junhong Shen, Tanya Marwah, and Ameet Talwalkar. Ups: Towards foundation models for pde solving via cross-modal adaptation, 2024.
- Qiang Shi and Eitan Geva. A new approach to calculating the memory kernel of the generalized quantum master equation for an arbitrary system–bath coupling. *The Journal of chemical physics*, 119(23):12063–12076, 2003.
- Makoto Takamoto, Timothy Praditia, Raphael Leiteritz, Dan MacKinlay, Francesco Alesiani, Dirk Pflüger, and Mathias Niepert. PDEBENCH: An extensive benchmark for scientific machine learnin. In *ICLR 2023 Workshop on Physics for Machine Learning*, 2023.

- Yi Tay, Mostafa Dehghani, Samira Abnar, Yikang Shen, Dara Bahri, Philip Pham, Jinfeng Rao, Liu Yang, Sebastian Ruder, and Donald Metzler. Long range arena: A benchmark for efficient transformers. *arXiv preprint arXiv:2011.04006*, 2020.
- Alasdair Tran, Alexander Mathews, Lexing Xie, and Cheng Soon Ong. Factorized fourier neural operators. In *The Eleventh International Conference on Learning Representations*, 2023.
- Ashish Vaswani, Noam Shazeer, Niki Parmar, Jakob Uszkoreit, Llion Jones, Aidan N Gomez, Łukasz Kaiser, and Illia Polosukhin. Attention is all you need. *Advances in neural information processing systems*, 30, 2017.
- Pauli Virtanen, Ralf Gommers, Travis E. Oliphant, Matt Haberland, Tyler Reddy, David Cournapeau, Evgeni Burovski, Pearu Peterson, Warren Weckesser, Jonathan Bright, Stéfan J. van der Walt, Matthew Brett, Joshua Wilson, K. Jarrod Millman, Nikolay Mayorov, Andrew R. J. Nelson, Eric Jones, Robert Kern, Eric Larson, C J Carey, İlhan Polat, Yu Feng, Eric W. Moore, Jake VanderPlas, Denis Laxalde, Josef Perktold, Robert Cimrman, Ian Henriksen, E. A. Quintero, Charles R. Harris, Anne M. Archibald, Antônio H. Ribeiro, Fabian Pedregosa, Paul van Mulbregt, and SciPy 1.0 Contributors. SciPy 1.0: Fundamental Algorithms for Scientific Computing in Python. *Nature Methods*, 17:261–272, 2020. doi: 10.1038/s41592-019-0686-2.
- Ming-Liang Zhang, Being J Ka, and Eitan Geva. Nonequilibrium quantum dynamics in the condensed phase via the generalized quantum master equation. *The Journal of chemical physics*, 125(4), 2006.
- Robert Zwanzig. Memory effects in irreversible thermodynamics. *Physical Review*, 124(4):983, 1961.
- Robert Zwanzig. *Nonequilibrium Statistical Mechanics*. Oxford University Press, New York, 2001. ISBN 9780195140187.

A Extended Related Work

Neural Operators. The Fourier Neural Operator (FNO) is a Neural Operator that performs a transformation in the frequency space of the input [Li et al., 2021a]. Other models have proposed different inductive biases for Neural Operators, including physics based losses and constraints [Li et al., 2021b], using Deep Equilibrium Model (DEQ) Bai et al. [2019] to design specialized architectures for steady-state (time-independent) PDEs Marwah et al. [2023], and using local message passing Graph Neural Networks (GNNs) [Gilmer et al., 2017, Kipf and Welling, 2016] based encoders to model irregular geometries [Li et al., 2020, 2024]. Other methodologies to solve for PDEs include methods like Gupta and Brandstetter [2023], Rahman et al. [2023] that use the U-Net [Ronneberger et al., 2015] type architectures and works like [Cao, 2021, Hao et al., 2023] that introduce different Transformer Vaswani et al. [2017] based neural solution operators for modeling both time-dependent and time-independent PDEs. While most of these methodology are designed for time-dependent PDEs, there is no clear consensus of how to model the past-states to predict future states, and most of these methods predict the PDE states over time in an auto-regressive way by conditioning the model on varying lengths of the past states Li et al. [2021a], Tran et al. [2023], Hao et al. [2023].

Foundation models. Lately, there have been community efforts towards creating large scale foundational models for modeling multiple PDE families [McCabe et al., 2023, Hao et al., 2024, Shen et al., 2024], and weather prediction Pathak et al. [2022], Lam et al. [2022]. We hope that our study is useful in informing the architectural design of future models.

B Network Architectures

Factorized Fourier Neural Operator (FFNO) (Tran et al. [2023]): This model is a refinement over the original Fourier Neural Operator (Li et al. [2021a]). Given a hidden dimension h and a spatial grid \mathcal{S} , its layers $\ell : \mathbb{R}^{|\mathcal{S}| \times h} \rightarrow \mathbb{R}^{|\mathcal{S}| \times h}$ are defined as:

$$\ell(v) = v + \text{Linear}_{h,h'} \circ \sigma \circ \text{Linear}_{h',h} \circ \mathcal{K}[v] \quad (15)$$

where σ is the GeLU activation function [Hendrycks and Gimpel, 2016] and h' is an expanded hidden dimension. \mathcal{K} is a kernel integral operator that performs a linear transformation in the frequency space. Denoting by FFT_α , IFFT_α are to the Discrete Fast Fourier Transform and the Discrete Inverse Fast Fourier Transform along dimension α [Cooley et al., 1969], it can be written as:

$$\mathcal{K}[v] = \sum_{\alpha \in \{1, \dots, d\}} \text{IFFT}[R_\alpha \cdot \text{FFT}_\alpha[v]]$$

for learnable matrices of weights $R_\alpha \in \mathbb{C}^{h^2 \times k_{\max}}$. k_{\max} is the maximum number of Fourier modes which are used in \mathcal{K} . We use all Fourier modes by setting $k_{\max} = \lfloor \frac{f}{2} \rfloor$.

In our experiments, The FFNO model consists of 4 FFNO layers. For experiments in 1D, the hidden dimensions are all 128 ($h_j = 128$ for $j = 0, 1, 2, 3$) and the expanded hidden dimension of FFNO’s MLP h' is $4 \cdot 128$. For experiments in 2D, the hidden dimensions are all 64 and the expanded hidden dimension is $4 \cdot 64$.

S4 - Factorized Fourier Neural Operator (s4FFNO): This model uses our MemNO framework. To discern the effect of memory, all layers except the memory layer will be the same as FFNO. For the memory layer, we choose an S4 layer Gu et al. [2022] with a state dimension of 64 and a diagonal S4 (S4D) kernel.³

For all our models, we use a simple spatial positional encoding E . In 1D, if the grid has f equispaced points in $[0, L]$, then $E \in \mathbb{R}^f$ and the positional encoding is defined as $E_i = \frac{i}{L}$ for $0 \leq i \leq f - 1$. In 2D, if we have a $f \times f$ points 2D equispaced grid in $[0, L_x] \times [0, L_y]$, the positional encoding is defined as $E_{ij} = (\frac{i}{L_x}, \frac{j}{L_y})$.

³The S4 repository has two available kernels, the diagonal S4 (S4D) and the Normal Plus Low Rank S4 (S4NPLR). In our experiments, we didn’t find a significant difference between the two, and chose S4D for simplicity.

In the input lifting operator \mathcal{R}_{in} , the input and the grid are stacked and a Linear layer from $\mathbb{R}^2 \rightarrow \mathbb{R}^{h_0}$ is applied element-wise. For the decoder \mathcal{R}_{out} , we use another Linear layer (without positional encoding).

C Burgers' Equation (1D): A study on low-resolution

The Burgers' equation with viscosity ν is a nonlinear PDE used as a modeling tool in fluid mechanics, traffic flow, and shock waves analysis. It encapsulates both diffusion and advection processes, making it essential for studying wave propagation and other dynamic phenomena. It is known for exhibiting a rich variety of behaviors, including the formation of shock waves and the transition from laminar to turbulent flow. The viscous Burgers' equation is written as:

$$u_t + uu_x = \nu u_{xx}$$

We used the publicly available dataset of the Burgers' equation in the PDEBench repository (Takamoto et al. [2023]) with viscosity e^{-3} , which is available at resolution 1024. We compare our models at resolutions 64, 128, 256, 512 and 1024 and show the results at figure 4a. As in the case of KS, s4FFNO outperforms FFNO, especially at low resolutions. Furthermore, we show the difference in nRMSE at each timestep in figure 4b. We observe that at the first timestep there is no difference between the two models - this makes sense because s4FFNO has the exact same architecture as FFNO for the first timestep. Yet as the initial condition is rolled out, there is more history of the trajectory and the difference between FFNO and s4FFNO increases.

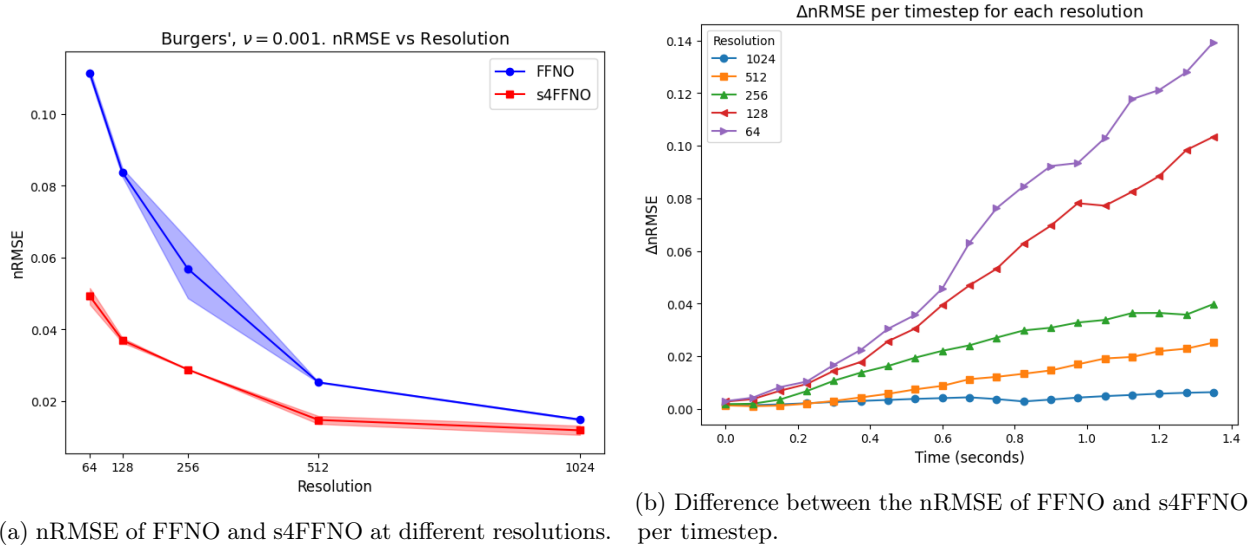


Figure 4: Results for the Burgers's PDEBench dataset with viscosity $\nu = 1e^{-3}$.

C.1 Relationship with fraction of unobserved information

As mentioned in Section 6.4 we measure the correlation of ω_f defined in Equation 14 with the difference in the nRMSE between FFNO and s4FFNO. The results can be seen in Figure 5

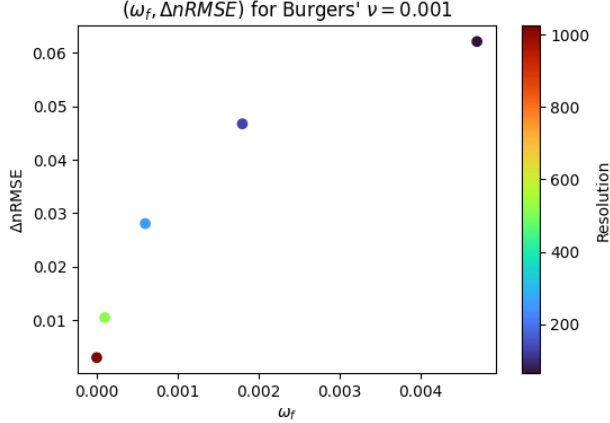


Figure 5: Values of ω_f (defined in Equation 14) and the difference in nRMSE between FFNO and s4FFNO for different resolutions in two of our experiments for Burgers’ Equation. ω_f is averaged over all trajectories in the dataset. The value is computed approximating the continuous Fourier modes with the Discrete Fourier modes of the solution in the highest resolution available (1024 for Burgers’ Equation).

D Data Generation

D.1 Kuramoto–Sivashinsky equation

For Kuramoto–Sivashinsky (KS) equation is given by:

$$\begin{aligned} u_t + uu_x + u_{xx} + \nu u_{xxxx} &= 0 \quad (t, x) \in [0, T] \times [0, L] \\ u(0, x) &= u_0(x) \quad x \in [0, L] \end{aligned}$$

We use periodic boundary conditions. Our data generation method is very similar to the one of [Brandstetter et al. \[2022\]](#). We employ the *method of lines* [[Schiesser, 1991](#)], where the spatial dimension is discretized, and the PDE is transformed to a systems of Ordinary Differential Equations (ODEs), one per point in the grid. In order to compute the spatial derivative of the solution at each point in the grid, a pseudospectral method is used, where derivatives are computed in frequency space and then converted to the original space through a Fast Fourier Transform. This method is implemented in the `diff` method of the `scipy.fftpack` package [[Virtanen et al., 2020](#)]. Similarly, the system of ODEs is solved numerically with a implicit Runge–Kutta method of the Radau IIA family of order 5 [[Hairer and Wanner, 1996](#)], which is implemented in the `solve_ivp` method of `scipy.integrate`. We refer to the code provided in [Brandstetter et al. \[2022\]](#) to reproduce this data generation, however certain small modifications have to be made, like using a fixed Δt per trajectory and increasing the number of modes in the initial condition.

As for the PDE parameters, we use $L = 64$ and $T = 5$. For the initial condition, we use a superposition of sinusoidal waves:

$$u_0(x) = \sum_{i=0}^{20} A_i \sin\left(\frac{2\pi k_i}{L}x + \phi_i\right)$$

where for each trajectory, the A_i are sampled from a continuous uniform in $[-0.5, 0.5]$, the k_i are sampled from a discrete uniform in $\{1, 2, \dots, 8\}$, and the ϕ_i are sampled from a uniform uniform in $[0, 2\pi]$. We discretize $[0, T]$ into 26 equispaced points separated by $\Delta t = 0.2^4$, keep the 25 temporal points generated by the numerical solver and discard our initial condition. In the experiments in section 6.2, for each of the four values of the viscosity (0.15, 0.125, 0.1, 0.075), we generated a dataset with spatial resolution 512 with 2048

⁴We reiterate that, as opposed to [[Brandstetter et al., 2022](#)], we don’t have a random Δt per trajectory

training samples and 256 test samples. For the experiment in the sequential model ablation in section F.1, we generated one dataset with viscosity 0.15 in resolution 256, 4096 training samples and 256 test samples.

D.2 Burgers' 1D equation

The 1D Burgers' equation can be written as:

$$u_t + uu_x = \nu u_{xx} \quad (t, x) \in [0, T] \times [0, L]$$

For the Burgers' equation, we take the publicly available Burgers' dataset of PDEBench [Takamoto et al., 2023] with viscosity 0.001. Out of the 10000 samples of the dataset, we use a 10% for testing. For training, we found it sufficient to use 2048 samples. Additionally, for training and testing we only used the 20 first timesteps, since we observed that after the 20th timestep the diffusion term of the equation u_{xx} attenuates all high frequencies and the solution changes very slowly.

D.3 Navier Stokes 2D equation

The incompressible Navier Stokes equation in the 2D unit torus is given by:

$$\begin{aligned} \frac{\partial w(x, t)}{\partial t} + u(x, t) \cdot \nabla w(x, t) &= \nu \Delta w(x, t) + f(x), & x \in (0, 1)^2, t \in (0, T] \\ \nabla \cdot u(x, t) &= 0, & x \in (0, 1)^2, t \in [0, T] \\ w(x, 0) &= w_0(x), & x \in (0, 1)^2 \end{aligned}$$

For the data generation, we follow the method of Li et al. [2021a], yet with different temporal and spatial grids. The initial conditions w_0 are sampled from a Gaussian Random field $\mathcal{N}\left(0, 7^{\frac{3}{2}}(-\Delta + 49I)^{-2.5}\right)$ with periodic boundary conditions. The forcing term is $f(x_1, x_2) = 0.1(\sin 2\pi(x_1 + x_2) + \cos 2\pi(x_1 + x_2))$. At each timestep, the velocity is obtained from the vorticity by solving a Poisson equation. Then, spatial derivatives are obtained, and the non-linear term is computed in the physical space and then dealiased. A Crank-Nicholson scheme is used to move forward in time, with a timestep of 10^{-4} . We use a 512x512 spatial grid which is then downsampled to 64x64 for our experiments. For the viscosity $\nu = 10^{-3}$, we use a final time of 16 seconds and sample every 0.5 seconds. For the viscosity $\nu = 10^{-5}$, we use a final time of 3.2 seconds and sample every 0.1 seconds. For more details on the data generation algorithm, we refer to Li et al. [2021a].

E Training details

In this section, we will provide a detailed description of the training hyperparameters used in the KS experiments of Section 6.2, in the Burgers experiments of section C and the Navier Stokes experiments of section 6.3. We start with the training hyperparameters. All our experiments used a learning rate of 0.001. For the number of epochs, in KS and Burgers, the training was done over 200 epochs with cosine annealing learning scheduling [Loshchilov and Hutter, 2017]; whereas in Navier Stokes we trained for 300 epochs and halved the learning rate every 90. As for the number of samples, KS and Burgers were trained with 2048 samples and Navier Stokes with 1024 samples. Lastly, we observed that the batch size was a sensitive hyperparameter for both the memory and memoryless models (it seemed to affect both equally) so we run a sweep at each experiment to select the best performing one. In the results shown in the paper, KS and Navier Stokes use a batch size of 32, and Burgers a batch size of 64.

Another relevant detail is the memory length in training, that is, the number of past states that were fed to the memory layer in the MemNO model. In the KS and Burgers experiments, the maximum memory length

was 25 (which is the same as the number of timesteps of the dataset). That means that for the last timestep, the previous 24 states were fed into the memory layer. However, for GPU memory limitations in Navier Stokes the memory length was 16, half the number of timesteps of each trajectory in the dataset. In this case, the memory was reset after the 16th timestep, i.e. for the 16th timestep the 15 past states were fed to the memory model, yet for the 17th timestep only the 16th timestep was fed. Then, for the 18th timestep, the 17th and 16th were fed, and so on.

As in [Tran et al., 2023], experiments were trained using teacher forcing. This means that for the prediction of the i -th timestep during training, the ground truth of the $i - 1$ previous steps was fed to the model (as opposed to the prediction of the model for such steps).

We run our experiments on A6000/A6000-Ada GPUs. The Navier Stokes 2D experiments required around 34GB of GPU memory for the batch size of 32 and took around 5 hours to finish, whereas the rest of experiments in 1D required a lower GPU memory (less than 10GB) and each run normally took less than an hour.

F Ablations on the Memory layer

In this section we present two ablations regarding the memory layer of MemNO.

F.1 Ablation: Choice of sequential model

In section 4.2 we introduced MemNO as an architecture framework which allowed the introduction of memory through any choice of a sequential layer, which we chose as S4 in the previous experiments. In this section, we explore two other candidates for the sequential layers: a transformer and an LSTM. We introduce **Transformer-FFNO (T-FFNO)** and **LSTM-FFNO** as two models that are identical to s4FFNO except in the sequential layer, where a transformer and an LSTM are used respectively. The LSTM model only has one layer and the transformer layer includes causal masking and a positional encoding. The positional encoding for pos across the time dimension and i across the hidden dimension is given by:

$$PE(pos, 2i) = \sin\left(\frac{pos}{10000^{\frac{2i}{\dim_{\text{model}}}}}\right)$$

$$PE(pos, 2i + 1) = \cos\left(\frac{pos}{10000^{\frac{2i}{\dim_{\text{model}}}}}\right)$$

We show results for the KS dataset with viscosity $\nu = 0.15$ and different resolutions. This dataset was generated using a resolution of 256 and contains 4096 samples, twice as many compared to the KS datasets of D, given that transformers are known to perform better in high-data regimes. The results are shown in Figure 6. TFFNO performs significantly worse than s4FFNO across almost all resolutions, and even performs worse than FFNO. In contrast, LSTM-FFNO outperforms FFNO, which shows that MemNO can work with other sequential models apart from S4. The memory term in Equation 6 is a convolution in time, which is equivalent to the S4 layer and very similar to a Recurrent Neural Network (RNN) style layer, as showed in Gu et al. [2022]. We believe that this inductive bias in the memory layer is the reason why both s4FFNO and LSTM-FFNO outperform FFNO. However, S4 was designed with a bias for continuous signals and has empirically proven better performance in these kind of tasks [Gu et al., 2022], which is in agreement with its increased performance over LSTMs in this experiment. Additionally, we observed that LSTMs were unstable to train in Navier Stokes 2D datasets.

Lastly, we make two remarks. Firstly, we believe that transformers performed worse due to overfitting, given that the train losses were normally comparable or even smaller than the train losses of the rest of the models at each resolution. Modifications of the transformer model or to the training hyperparameters as in other works [Hao et al., 2024, Cao, 2021, Hao et al., 2023] might solve this issue. Secondly, recently there has been

a surge of new sequential models such as Mamba [Gu and Dao, 2023], RWQK [Peng et al., 2023], xLSTM [Beck et al., 2024] or LRU [Orvieto et al., 2023]. We leave it as future work to study which of these sequential model has better overall performance, and hope that our study on the settings where the memory effect is relevant can help make accurate comparisons between them.

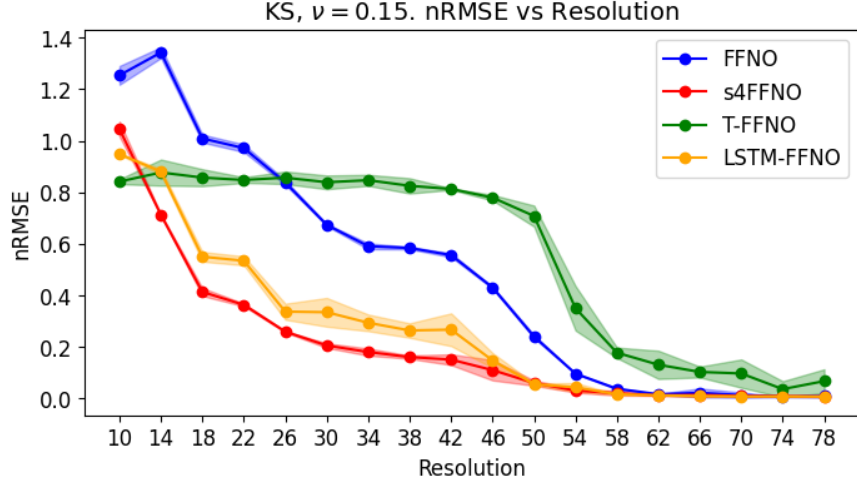


Figure 6: Performance of FFNO, s4FFNO and T-FFNO and LSTM-FFNO in KS with viscosity $\nu = 0.15$.

F.2 Ablation: memory layer configuration

In Section 4.2 we introduced the memory layer in MemNO as a single layer to be interleaved with Neural Operator layers. In our experiments, we inserted it after the second layer of a four layer Neural Operator. In this section, we explore the impact of having different layer configurations, including the possibility of having several memory layers. We will denote the configurations with a sequence of S and T letters. S means a Neural Operator layer (some sort of Spatial convolution), and T a memory layer (some sort of Time convolution). For example, *SSTSS* denotes the architecture of our experiments, where we have 2 Neural Operators layers, followed by a memory layer, followed by other 2 Neural Operator layers. Similarly, *SSSST* denotes 4 Neural Operators layers followed by a memory layer. In Table 2, we present the results for the KS dataset with $\nu = 0.1$ and final time of 4 seconds for several models. We include the s4FFNO model we used in previous experiments in the first row (with configuration *SSTSS*), and the FFNO model in the last row. In the middle rows, we show different configurations of memory and Neural Operator layers. It can be observed that all models with at least a memory layer outperform FFNO. There are slight differences between configurations, yet we focused mainly on the comparison to the memoryless model. For that reason, we fixed *SSTSS* configuration in our previous experiment, which was the most efficient (only one memory layer) and symmetric. We leave as further work determining if there are settings where a given configuration pattern can be substantially better than the rest.

Architecture	nRMSE ↓		
	Resolution 32	Resolution 48	Resolution 64
s4FFNO (<i>SSTSS</i>)	0.123 ± 0.011	0.086 ± 0.004	0.015 ± 0.001
s4FFNO (<i>SSSST</i>)	0.142 ± 0.009	0.069 ± 0.001	0.017 ± 0.001
s4FFNO (<i>STSSST</i>)	0.141 ± 0.006	0.064 ± 0.002	0.019 ± 0.001
s4FFNO (<i>STSTSTST</i>)	0.113 ± 0.006	0.070 ± 0.004	0.017 ± 0.001
s4FFNO (<i>TSSSS</i>)	0.129 ± 0.007	0.080 ± 0.003	0.017 ± 0.001
FFNO	0.294 ± 0.004	0.138 ± 0.013	0.021 ± 0.002

Table 2: KS, $\nu = 0.1$. The final time is 4 seconds and the trajectories contain 20 timesteps. For each architecture, we tried 4 learning rates (0.002, 0.001, 0.0005 and 0.00025, each with three different seeds. We present the results of the learning rate with the lowest nRMSE averaged across the three seeds. The standard deviation is also with respect to the seeds.

G Appendix: Quantifying the effect of memory

Proof. We proceed to the Equation 10 first. Note that $u_1(t), \forall t \geq 0$ can be written as $u_1(t) = a_0^{(t)}\mathbf{e}_0 + a_1^{(t)}\mathbf{e}_1$. Moreover, by Proposition 1, we have

$$\frac{\partial a_0^{(t)}}{\partial t} = 2Ba_1^{(t)} \quad (16)$$

$$\frac{\partial a_1^{(t)}}{\partial t} = a_1^{(t)} + Ba_0^{(t)} \quad (17)$$

In matrix form, these equations form a linear matrix ODE:

$$\frac{\partial}{\partial t} \begin{pmatrix} a_0^{(t)} \\ a_1^{(t)} \end{pmatrix} = \begin{pmatrix} 0 & 2B \\ B & 1 \end{pmatrix} \begin{pmatrix} a_0^{(t)} \\ a_1^{(t)} \end{pmatrix}$$

The solution of this ODE is given by $\begin{pmatrix} a_0^{(t)} \\ a_1^{(t)} \end{pmatrix} = \exp\left(t \begin{pmatrix} 0 & 2B \\ B & 1 \end{pmatrix}\right) \begin{pmatrix} a_0^{(0)} \\ a_1^{(0)} \end{pmatrix}$. By the first statement of Lemma 1 and the non-negativity of $a_0^{(0)}, a_1^{(0)}$, we get:

$$a_0^{(t)} \leq 10e^{\sqrt{2}Bt} \left(a_0^{(0)} + a_1^{(0)}\right), \quad (18)$$

$$a_1^{(t)} \leq 10e^{\sqrt{2}Bt} \left(a_0^{(0)} + a_1^{(0)}\right) \quad (19)$$

We proceed to Equation 11. Note that for any $s \geq 0$, we can write $u_2(s) = \hat{a}_0^{(s)}\mathbf{e}_0 + \hat{a}_1^{(s)}\mathbf{e}_1$ with $\hat{a}_0^{(0)} = a_0^{(0)}$ and $\hat{a}_1^{(0)} = a_1^{(0)}$. By Proposition 1, we have

$$\mathcal{QL}u_2(x) = B\hat{a}_1^{(s)}\mathbf{e}_2(x)$$

Moreover, given a function $v(x)$, the action of the operator $\exp\{\mathcal{QL}(\tilde{t})\}$ on v is given by the solution $w(\tilde{t}, x)$ to the PDE

$$\begin{aligned} \frac{\partial}{\partial t} w(t, x) &= \mathcal{QL}w(t, x) \\ w(0, x) &= v(x) \end{aligned}$$

If $w(t, x) = \sum_{n \in \mathbb{N}_0} b_n^{(t)}\mathbf{e}_n$ and $\forall n \in \mathbb{N}_0, b_n^{(0)} \geq 0$, we are interested in solving the previous PDE with initial conditions $b_2^{(0)} = B\hat{a}_1^{(s)}$ and $b_n^{(0)} = 0 \forall n \neq 2$.

We claim that the coefficients $\hat{a}_n^{(t)} \geq 0 \forall t > 0$ and $\forall n \in \{0, 1\}$. For $t = 0$ this is by definition, and we will prove it for all t by way of contradiction. Suppose the claim is not true, then there exists a $t^* > 0$, and some $n^* \in \{0, 1\}$ such that $\hat{a}_{n^*}^{(t^*)} = 0$, and $\hat{a}_n^{(s)} > 0 \forall n \in \{0, 1\}$ and $\forall s < t^*$. But from continuity this implies that there exists $0 < t' < t^*$ such that $\frac{\partial}{\partial t} \hat{a}_{n^*}^{(t')} < 0$. However, it can be easy to see that if $\hat{a}_n^{(s)} > 0 \forall s \leq t'$, then $\mathcal{P}_1 \mathcal{L} u_2(t') > 0$ and $\mathcal{P}_1 \mathcal{L} \int_0^{t'} \exp\{\mathcal{Q}\mathcal{L}(t-s)\} u_2(s) ds > 0$. Therefore, from Equation 11, $\frac{\partial}{\partial t} \hat{a}_{n^*}^{(t')} > 0$, which is a contradiction.

This claim implies that $b_n^{(0)} \geq 0 \forall n \in \mathbb{N}$, and in turn it implies that $b_n^{(t)} \geq 0 \forall n \in \mathbb{N}, t > 0$. Applying $\mathcal{Q}\mathcal{L}$ results in the following inequalities for the coefficients $b_1^{(t)}, b_2^{(t)}, b_3^{(t)}$:

$$\frac{\partial}{\partial t} b_1^{(t)} \geq b_1^{(t)} + B b_2^{(t)} \geq B b_2^{(t)} \quad (20)$$

$$\frac{\partial}{\partial t} b_2^{(t)} \geq B b_1^{(t)} + 4 b_2^{(t)} + B b_3^{(t)} \geq B b_1^{(t)} + B b_3^{(t)} \quad (21)$$

$$\frac{\partial}{\partial t} b_3^{(t)} \geq B b_2^{(t)} + 9 b_3^{(t)} \geq B b_2^{(t)} \quad (22)$$

Thus, we can write a linear matrix ODE for the vector $(b_1^{(t)}, b_2^{(t)}, b_3^{(t)})$:

$$\frac{\partial}{\partial t} \begin{pmatrix} b_1^{(t)} \\ b_2^{(t)} \\ b_3^{(t)} \end{pmatrix} \geq \begin{pmatrix} 0 & B & 0 \\ B & 0 & B \\ 0 & B & 0 \end{pmatrix} \begin{pmatrix} b_1^{(t)} \\ b_2^{(t)} \\ b_3^{(t)} \end{pmatrix} \quad (23)$$

Therefore, using Lemma 2, for sufficiently large B we have $b_2^{(t-s)} \geq \frac{B e^{\sqrt{2} B (t-s)}}{10} \hat{a}_1^{(s)}$.

Hence, if we write $\int_0^t \exp\{\mathcal{Q}\mathcal{L}(t-s)\} \mathcal{Q}\mathcal{L} u_2(s) ds$ in the basis $\{\mathbf{e}_n\}_{n \in \mathbb{N}_0}$, the coefficient for \mathbf{e}_2 will be lower bounded by

$$\int_0^t \frac{1}{10} B e^{B(t-s)} a_1^{(s)} ds$$

Applying the second statement of Lemma 1 and using the non-negativity of $a_0^{(0)}$ and $a_1^{(0)}$, we have $\hat{a}_1^{(s)} \geq \frac{1}{10} e^{\sqrt{2} B s} (a_0^{(0)} + a_1^{(0)})$. Hence, the coefficient for \mathbf{e}_2 is lower bounded by

$$\int_0^t \frac{1}{10} B e^{\sqrt{2} B (t-s)} \frac{1}{10} e^{\sqrt{2} B s} (a_0^{(0)} + a_1^{(0)}) ds \geq \frac{B t}{100} e^{\sqrt{2} B t} (a_0^{(0)} + a_1^{(0)})$$

We finally need to consider what happens after applying the outermost operator $\mathcal{P}_1 \mathcal{L}$. Because of Proposition 1 again, applying \mathcal{L} makes the coefficient in front of \mathbf{e}_1 at least $\frac{B^2 t}{100} e^{\sqrt{2} B t} (a_0^{(0)} + a_1^{(0)})$. Finally, applying \mathcal{P}_1 preserves the coefficient in front of \mathbf{e}_1 .

Hence, equation Equation 11 results in the following evolution inequalities:

$$\frac{\partial \hat{a}_0^{(t)}}{\partial t} \geq 2 B \hat{a}_1^{(t)} \quad (24)$$

$$\frac{\partial \hat{a}_1^{(t)}}{\partial t} \geq \hat{a}_1^{(t)} + B \hat{a}_0^{(t)} + \frac{B^2 t}{100} e^{\sqrt{2} B t} (a_0^{(0)} + a_1^{(0)}) \quad (25)$$

Using the second statement of Lemma 1 again we have that $\hat{a}_0(t) \geq \frac{1}{10} e^{\sqrt{2} B s} (a_0^{(0)} + a_1^{(0)})$. Thus, dropping the (positive) term $\hat{a}_1^{(t)}$ in equation 25, we have:

$$\frac{\partial \hat{a}_1^{(t)}}{\partial t} \geq \left(\frac{1}{10} + \frac{B t}{100} \right) B e^{\sqrt{2} B t} (a_0^{(0)} + a_1^{(0)}) \quad (26)$$

Integrating this equations yields:

$$\hat{a}_1^{(t)} \geq a_1^{(0)} + \frac{1}{200} e^{\sqrt{2}Bt} \left(\sqrt{2}Bt + 10\sqrt{2} - 1 \right) \left(a_0^{(0)} + a_1^{(0)} \right) \quad (27)$$

Thus, we have $a_1^{(t)} \gtrsim Bte^{\sqrt{2}Bt} \left(a_0^{(0)} + a_1^{(0)} \right)$. Together with equation 18, the claim of the Theorem follows. \square

Lemma 1. *There exists $B > 0$ sufficiently large such that for all $t > 0$ the matrix $\begin{pmatrix} 0 & 2Bt \\ Bt & t \end{pmatrix}$ satisfies:*

$$\forall i, j \in \{1, 2\}, \exp \left(\begin{pmatrix} 0 & 2Bt \\ Bt & t \end{pmatrix} \right)_{i,j} \leq 10 \exp(\sqrt{2}Bt) \quad (28)$$

$$\forall i, j \in \{1, 2\}, \exp \left(\begin{pmatrix} 0 & 2Bt \\ Bt & t \end{pmatrix} \right)_{i,j} \geq \frac{1}{10} \exp(\sqrt{2}Bt) \quad (29)$$

Proof. By direct calculation, we have:

$$\exp \left(\begin{pmatrix} 0 & 2Bt \\ Bt & t \end{pmatrix} \right) = \frac{1}{2\sqrt{8B^2+1}} \begin{pmatrix} \sqrt{8B^2+1}g(B,t) - h(B,t) & 4Bh(B,t) \\ 2Bh(B,t) & \sqrt{8B^2+1}g(B,t) + h(B,t) \end{pmatrix}$$

where:

$$\begin{aligned} g(B,t) &= e^{\frac{1}{2}(\sqrt{8B^2+1}+1)t} + e^{-\frac{1}{2}(\sqrt{8B^2+1}-1)t} \\ h(B,t) &= e^{\frac{1}{2}(\sqrt{8B^2+1}+1)t} - e^{-\frac{1}{2}(\sqrt{8B^2+1}-1)t} \end{aligned}$$

Thus, the statement follows. \square

Lemma 2. *For all $B > 0$, the matrix $\begin{pmatrix} 0 & B & 0 \\ B & 0 & B \\ 0 & B & 0 \end{pmatrix}$ satisfies:*

$$\forall i, j \in \{1, 2, 3\}, \exp \left(\begin{pmatrix} 0 & B & 0 \\ B & 0 & B \\ 0 & B & 0 \end{pmatrix} \right)_{i,j} \geq \frac{1}{10} \exp(\sqrt{2}B) \quad (30)$$

Proof. By direct calculation:

$$\begin{aligned} \exp \left(\begin{pmatrix} 0 & B & 0 \\ B & 0 & B \\ 0 & B & 0 \end{pmatrix} \right)_{i,j} &= \\ \frac{1}{4} e^{-\sqrt{2}B} &\begin{pmatrix} 2e^{\sqrt{2}B} + e^{2\sqrt{2}B} + 1 & \sqrt{2}e^{2\sqrt{2}B} - \sqrt{2} & -2e^{\sqrt{2}B} + e^{2\sqrt{2}B} + 1 \\ \sqrt{2}e^{2\sqrt{2}B} - \sqrt{2} & 2(e^{\sqrt{2}B} + 1) & \sqrt{2}e^{2\sqrt{2}B} - \sqrt{2} \\ -2e^{\sqrt{2}B} + e^{2\sqrt{2}B} + 1 & \sqrt{2}e^{2\sqrt{2}B} - \sqrt{2} & 2e^{\sqrt{2}B} + e^{2\sqrt{2}B} + 1 \end{pmatrix} \end{aligned}$$

Thus, the statement follows. \square